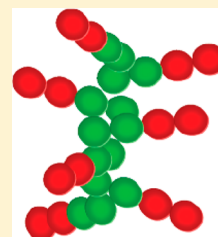


# Theoretical Study of the Structure and Assembly of Janus Rods

Mukta Tripathy<sup>†,‡</sup> and Kenneth S. Schweizer<sup>\*,‡,§,||</sup><sup>†</sup>Department of Chemical and Biomolecular Engineering, <sup>§</sup>Department of Materials Science, and <sup>||</sup>Frederick Seitz Materials Research Laboratory, University of Illinois, 1304 West Green Street, Urbana, Illinois 61801, United States

**ABSTRACT:** Microscopic integral equation theory is applied to investigate the real and Fourier space structure and phase behavior of compositionally symmetric AB Janus rods that interact via hard core excluded volume interactions and competing repulsive and attractive tail potentials. If the spatial range of the latter are short and equal, chemical asymmetry results in attraction-driven assembly into a cylindrical micellar structure of spatial periodicity between one and two rods lengths. The apparent microphase spinodal ordering temperature increases with attraction range and rod length, and the microdomain coherence length strongly grows upon cooling. However, as the tail repulsion range increases significantly, the micellar morphology is destroyed and a new repulsion-driven ordering emerges at high volume fractions characterized by a much smaller spatial periodicity. We also find a tight correlation between the local attraction-induced clustering (quantified by the excess number of nearest neighbors) and the microdomain-scale ordering (measured by the amplitude of the intense low wavevector peak of the collective structure factor). Moreover, the former converges to a unique value at the microphase spinodal temperature for all volume fractions, repulsion strengths, and tail repulsion ranges studied, in qualitative contrast to the behavior of the repulsive-interaction driven ordering phenomena. The phase behavior trends of the integral equation approach are compared to a computationally and conceptually simpler mean field hybrid formulation based on a random phase approximation treatment of tail potentials, thereby allowing the role of physical clustering, interparticle correlations, and microdomain scale concentration fluctuations to be assessed.



## I. INTRODUCTION

Over the past decade, much progress has been made in the synthesis<sup>1–6</sup> and study of chemically heterogeneous AB Janus spheres via experiment,<sup>7,8</sup> theory,<sup>9,10</sup> and computer simulation.<sup>8,11,12</sup> The simplest Janus particle consists of two chemically distinct hemispheres, where typically one side is hydrophilic and experiences repulsive interactions in a polar solvent such as water, and the other side is hydrophobic, which experiences attractive interactions. de Gennes viewed such objects as solid surfactants.<sup>13</sup> Janus colloids find applications as membrane reactors,<sup>14</sup> switchable display panels,<sup>1</sup> self-motile systems,<sup>15,16</sup> biochemical sensors,<sup>17</sup> and tiny rheometers.<sup>18</sup> An analogous class of materials are block copolymers, where the enthalpy-driven clustering of chemically similar monomers and the constraint of chain connectivity results in a large array of microphase structures.<sup>19–23</sup> In colloid science, particles with isotropic pair potentials have also been theoretically predicted,<sup>24</sup> and observed in experiment and simulation,<sup>25</sup> to undergo microphase separation due to a competition between a strong short-range attraction and longer range repulsion.

The chemical asymmetry of Janus particles implies strongly anisotropic interactions that can result in new crystalline or microphase-ordered structures, complex phase diagrams, and unusual clusters.<sup>8,11,26</sup> Most recently, “triblock” ABA striped spheres have been discovered to self-assemble into novel structures, such as the Kagome lattice,<sup>27,28</sup> and complementary simulations<sup>27,29</sup> have been performed. More generally, the growing ability<sup>30</sup> to control “Janus balance” (amount of A and B) and patch geometry on a colloidal surface promises the discovery, in the near future, of many more novel colloidal structures.

Janus rigid rods are perhaps the simplest class of particles that combine shape and chemical anisotropy. Several recent efforts have been made to synthesize them and study their assembly,<sup>31–33</sup> and their application in self-motility<sup>34</sup> and controlling block copolymer assembly<sup>35</sup> have been suggested. Magnetic Janus rods can be utilized for payload capture<sup>36</sup> and patchy nanorods as catalytic nanomotors,<sup>37</sup> fluorescent barcodes,<sup>38</sup> and in electrical sensing.<sup>39</sup> Biologically, patchy rod-like BAR proteins insert themselves in the cell membrane to control cell shape, growth, adhesion, and motility via curvature-induced invaginations.<sup>40,41</sup>

In contrast to the self-assembly of block copolymers, flexible chain surfactants, microemulsions, and other soft material systems,<sup>42</sup> progress in developing a theoretical understanding of Janus colloids is in a very early stage. One reason is that microphase separation or micelle formation in the former systems generally occurs on the global molecular scale, not the very local monomer scale where intermolecular interactions operate. This separation of length scales allows coarse graining procedures to be applied, which greatly simplifies the theoretical description. For example, in block copolymer melts, the singular short-range intermonomer excluded volume repulsions are mimicked by a long wavelength incompressibility constraint, while the relatively weak van der Waals attractions are mimicked via a single phenomenological Flory chi-parameter.<sup>43</sup> Such “mean field” approaches neglect interchain correlations. In contrast, the self-assembly of Janus colloids

Received: September 10, 2012

Revised: October 24, 2012

Published: December 4, 2012

involves confronting particle rigidity, strong packing correlations, short-range attractions, and coupled structural fluctuations from the site (monomer) size scale upward. As true for the crystallization of atomic and molecular liquids,<sup>44</sup> there is often no clear separation between local and ordering length scales.

The above considerations suggest a liquid state physics approach may be fruitful for beginning to understand suspensions of Janus colloids. Here we employ the well-known Reference Interaction Site Model (RISM) integral equation approach<sup>45</sup> to study relatively short, compositionally balanced AB Janus rods. To the best of our knowledge, the only other attempt to use RISM theory for Janus-like objects has been for AB Janus spheres and a patchy tetrahedral network forming model.<sup>46</sup> We employ both the numerically intensive RISM theory that includes spatial correlations on all length scales and a simplified limit inspired by polymer mean field theories where hard core repulsions and tail potentials are treated in very different ways. We refer to the latter as the hybrid RISM-RPA approach,<sup>26</sup> where RPA stands for “random phase approximation”. By contrasting the predictions of these two approaches, one can gain insight concerning the full consequences of the excluded volume and nonbonded interactions on assembly. Although integral equation theories cannot predict the lattice symmetry of microphase separated structures, their ability to compute the full correlated statistical microstructure over all length scales allows educated inferences to be made concerning at least the local geometry of the building blocks that lead to microphase ordering, as recently demonstrated in the tetrahedral colloid RISM study.<sup>46</sup>

Section II presents the models employed, RISM theory for Janus rods, and sample calculations that illustrate how phase transitions are treated. In section III, intermolecular correlations, scattering patterns, and phase behavior of Janus rods are studied, including attraction and repulsion driven microphase separation. The effect of rod aspect ratio and variable interparticle potentials are explored in section IV. Section V presents the hybrid RISM-RPA approach and representative calculations. Conclusions are drawn in section VI.

## II. MODELS AND RISM THEORY

**A. Interaction Potentials.** The AB Janus rod is modeled as a set of linearly and tangentially connected spherical interaction sites of identical hard core diameters,  $\sigma$ . In general, each site interacts via a hard core repulsion and a tail potential. As indicated in Figure 1, the repulsive sites (red) are denoted as  $a$ , and attractive sites (green) are denoted as  $b$ . We focus primarily on 4-site Janus rods of  $aabb$  “diblock” architecture. Unless otherwise stated, the tail potentials are taken to be of a square well (square step) form of range  $\alpha_b$  for  $b$ -sites ( $\alpha_a$  for  $a$ -sites), with repulsive (attractive) strength at contact of  $\epsilon_a$  ( $\epsilon_b$ ) reported in units of the thermal energy,  $k_B T$ . The  $a$ – $b$  interactions are “neutral”, a purely hard core repulsion. An implicit solvent model is adopted. This choice of interaction potentials defines our “baseline” model and is meant to mimic a system where uncharged  $b$ -sites experience a short-range attraction (e.g., hydrophobic), charged  $a$ -sites experience a short-range (e.g., Coulombic) repulsion. Although the bare hard core site diameters are all identical, the presence of tail repulsions results in nonadditive excluded volume packing effects which can have significant consequences on assembly. Janus particle density is quantified by a volume fraction,  $\phi = \rho V_m$ , where  $\rho$  is the molecular number density and  $V_m$  is the

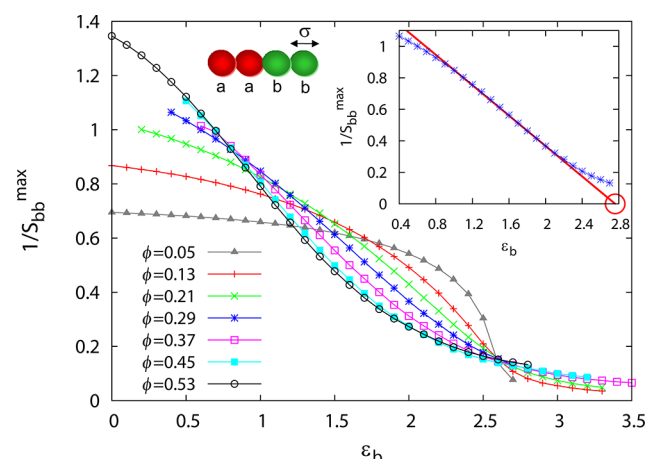


**Figure 1.** At the top left is an illustration of a Janus rod of aspect ratio four. The red (black, in grayscale)  $a$ -sites are repulsive and the green  $b$ -sites (gray, in grayscale) are attractive. The cross  $a$ – $b$  interaction is purely hard-core. The main panel shows calculations of the inverse value of the intensity of the fastest rising partial structure factor peak as a function of attraction strength, for  $aabb$  Janus rods at  $\epsilon_a/\epsilon_b = 1$  and  $\alpha_a = \alpha_b = 0.1\sigma$ , for various volume fractions. The inset shows the method of linear extrapolation used to determine the spinodal microphase separation temperature for  $\phi = 0.29$ .

space-filling hard core molecular volume. A smaller number of calculations for 8-site rods, and a Yukawa repulsive tail, are presented in section IV to test the sensitivity of our conclusions to these variables.

**B. RISM Theory of Janus Rods.** Calculations are performed using the RISM approach to determine the equilibrium structure and estimate (via spinodal extrapolation) microphase separation, and also a cruder “mean field” RISM-RPA theory where the effect of tail interactions are treated perturbatively.<sup>26</sup> Our primary focus is the former approach, which we now discuss.

The RISM theory of Chandler and Andersen<sup>44,45</sup> computes the equilibrium intermolecular structure of isotropic, globally homogeneous liquids of rigid particles composed of bonded spherical sites that interact via pair decomposable potentials. Particle shape is encoded via a matrix of intramolecular pair distribution functions,  $\mathbf{\Omega}(r)$ . The generalized matrix Ornstein–Zernike integral equation in Fourier space for a fluid is

$$\mathbf{H}(k) = \mathbf{\Omega}(k)\mathbf{C}(k)\mathbf{\Omega}(k) + \mathbf{\Omega}(k)\mathbf{C}(k)\mathbf{H}(k) \quad (1)$$

The elements of these matrices  $H_{MM'}(k) = \rho_M \rho_{M'} h_{MM'}(k)$ ,  $\Omega_{MM'}(k)$ , and  $C_{MM'}(k)$  are, respectively, the Fourier transforms of the density-scaled pair correlation function ( $g_{MM'}(r) = 1 + h_{MM'}(r)$ ), the density-scaled intramolecular distribution function, and the direct correlation function between sites of type  $M$  and  $M'$ . Here  $\rho_M = N_M \rho$  is the number density of sites of type  $M$ ,  $N_M$  is the number of sites of type  $M$ , and  $\rho$  is the number density of Janus rods. Assuming the sites of identical chemical nature are statistically equivalent (neglecting, or “pre-averaging”, rod end, or AB junction packing effects), eq 1 reduces to a  $2 \times 2$  matrix relation. This site equivalency simplification is standard in the application of RISM theory to polymers (homopolymers, blends, block copolymers).<sup>47</sup>

The matrix of partial static structure factors,  $\mathbf{S}(k)$ , is the Fourier transform of the corresponding (partial) density–density fluctuation correlation functions. Spinodal macrophase separation is identified by the simultaneous divergence of all

partial structure factors at zero wavevector ( $k^* = 0$ ) corresponding to an infinite compressibility. RISM theory does not predict first order phase transitions due to its self-consistent incorporation of fluctuation effects.<sup>47,48</sup> This is in contrast to cruder RPA-based approaches, including field theoretic approaches employed for polymeric systems,<sup>43,49</sup> where microphase separation can be identified by a (hypothetical) divergence of all partial structure factors at a finite “ordering” wavevector ( $k^* \neq 0$ ). The matrix of static structure factors is given by

$$\mathbf{S}(k) = [\mathbf{1} - \mathbf{\Omega}(k)\mathbf{C}(k)]^{-1}\mathbf{\Omega}(k) \quad (2)$$

The real space intramolecular distribution function between site  $\nu$  of type  $M$ , and site  $\gamma$  of type  $M'$  of the rigid Janus rod, is  $\omega_{\nu M \gamma M'}(r) = \delta(r - |\vec{r}_{\nu M \gamma M'}|)$ , where  $\vec{r}_{\nu M \gamma M'}$  is the distance between  $\nu$  and  $\gamma$ . The Fourier transform of this function is

$$\omega_{\nu M \gamma M'}(k) = \frac{\sin|\vec{r}_{\nu M \gamma M'}|k}{|\vec{r}_{\nu M \gamma M'}|k} \quad (3)$$

For the 4-site *aabb* Janus rod,

$$\Omega_{aa}(k) = \rho \omega_{aa}(k) = \rho \sum_{\nu, \gamma=1}^{N_a} \omega_{\nu a \gamma a}(k) = \rho 2 \left( 1 + \frac{\sin k\sigma}{k\sigma} \right) \quad (4)$$

$$\begin{aligned} \Omega_{ab}(k) &= \rho \omega_{ab}(k) \\ &= \rho \sum_{\nu=1}^{N_a} \sum_{\gamma=1}^{N_b} \omega_{\nu a \gamma b}(k) \\ &= \rho \left( \frac{\sin k\sigma}{k\sigma} + 2 \frac{\sin 2k\sigma}{2k\sigma} + \frac{\sin 3k\sigma}{3k\sigma} \right) \end{aligned} \quad (5)$$

Equation 1 involves a set of two unknown functions, ( $\mathbf{H}(k)$  and  $\mathbf{C}(k)$ ), and to solve them, we use the site–site Percus–Yevick (PY)<sup>50</sup> closure,

$$C_{ij}(r) = (1 - e^{U_{ij}(r)})(h_{ij}(r) + 1) \quad (6)$$

where  $U_{ij}(r)$  is the total pair potential in units of thermal energy between two sites of type  $i$  and  $j$ . Although the choice of closure approximation can be a subtle problem,<sup>44</sup> especially for self-assembling or phase separating flexible chain polymer systems,<sup>47</sup> we believe that for the one-component rigid molecular system interacting via short-range potentials of present interest, the PY approximation is an appropriate choice for this initial study. The coupled integral equations are numerically solved using a standard iterative algorithm,<sup>44,48</sup> the convergence of which determines how low in temperature we report results.

**C. Phase Behaviors.** Phase diagrams will be presented in the reduced temperature ( $T/\varepsilon_b$ )–volume fraction ( $\phi$ ) plane for various repulsion-to-attraction strength ratios ( $\varepsilon_a/\varepsilon_b$ ). Microphase separation is not literally predicted by RISM theory, and can only be estimated in an effective spinodal spirit by performing a linear extrapolation to zero of the inverse value of the fastest rising (typically low angle) structure factor peak. The extrapolation is performed based on the existence of a (higher reduced temperature) regime where this inverse peak value is a linear function of the dimensionless attraction strength, as illustrated by the inset of Figure 1. The spinodal point corresponds to the value of the attraction strength at which the inverse peak value of the structure factor linearly extrapolates to

zero. This is the standard approach to determining the mean field spinodal microphase transition based on a theory such as RISM,<sup>47,48</sup> where correlated concentration fluctuations destroy strict spinodal divergences at nonzero wavevector.<sup>51</sup> Though crude, such a procedure produces reasonable results for microphase separation transitions in diblock and multiblock copolymers<sup>47</sup> and the self-assembly of tethered chain nanoparticles.<sup>48</sup> Moreover, it corresponds to the operational procedure for extracting microphase spinodals based on small angle scattering data or polymer mean field theory.<sup>43,49</sup>

We note that, as a matter of principle, RISM theory can predict  $k = 0$  macrophase separation. Of course, in practice, this must also be analyzed numerically, and the same extrapolation procedure explained above is employed. Such macrophase separation transitions are in the liquid–gas category.

The inset of Figure 1 illustrates the microphase spinodal determination procedure for the *aabb* Janus rod system at  $\phi = 0.29$  and  $\varepsilon_a/\varepsilon_b = 1$ . In a literal mean field theory,<sup>43</sup> one expects the plot is linear for all inverse temperatures. In reality, this is not seen in scattering experiments, simulations, or theories that include fluctuation effects. Because RISM contains correlations over all length scales, one expects the nonlinear “bending over” seen in Figure 1 corresponding to fluctuation stabilization of the disordered phase via strong physical clustering.<sup>48,51</sup> Although the example shown in the inset has a well-defined and broad linear (as a function of inverse temperature) regime, the main panel of Figure 1 shows the former can be absent at lower volume fractions due to compressibility-magnified fluctuation effects. Hence, the extrapolation is less reliable at low volume fractions, which limits the Janus rod concentrations we analyze.

Crystallization on the monomer (site diameter) scale cannot be reliably treated based solely on integral equation theory. Rather, density functional or other methods are required.<sup>44</sup> However, oversimplified treatments are sometimes employed<sup>24,26,43</sup> based on the RPA-like scheme to crudely address thermally driven crystallization, as discussed in section V.

Liquid–gas macrophase separation ( $k = 0$ ) for Janus rods is expected to be highly frustrated because the A and B sites are chemically bonded. Unless stated otherwise, macrophase separation is absent or occurs at lower temperatures than studied. But to illustrate this phenomenon, Figure 2 shows calculations for the purely attractive *homogeneous* 4-site rods that interact via a square well attraction of range  $0.1\sigma$ . One sees an asymmetric demixing curve and a critical point at low volume fractions, features typical of macromolecular solutions.<sup>52</sup>

### III. SHORT JANUS RODS

Microphase separation has been widely studied in block-copolymer (BCP) melts<sup>53</sup> where monomer-rich A and B microdomains self-organize on lattices of mesoscopic periodicity and a symmetry that depends on polymer chain length, fraction of A monomers and temperature. Before presenting our Janus rod calculations, it is instructive to discuss how they differ from copolymers. (i) Janus rods are short rigid objects, not thin, long interpenetrating flexible coils. (ii) Both strong and spatially short-range tail repulsions (*a*-sites) and attractions (*b*-sites) typically exist associated with, for example, charge repulsions and hydrophobic attraction. This contrasts with common BCPs where weak van der Waals attractions determine a single chi-parameter.<sup>43,52</sup> (iii) Short Janus rods have large site-level excluded volume constraints on a scale



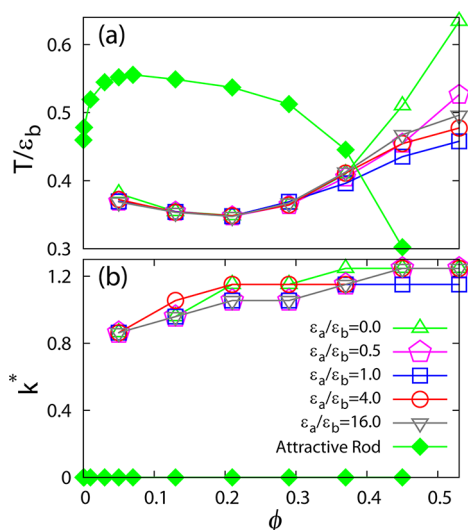


**Figure 2.** Spinodal phase diagrams for macrophase separation of homogeneous attractive rods of aspect ratio 4 (solid symbols) and microphase separation of Janus rods (open symbols). (a) Reduced macrophase (solid diamonds) and microphase (open symbols) separation temperatures of a fluid of attractive (Janus) rods, with  $\alpha = 0.1\sigma$  ( $\alpha_a = \alpha_b = 0.1\sigma$ ); the different open symbols correspond to different values of the ratio of attraction to repulsion strength at contact, as defined in the legend of (b). Above each curve the system is a homogeneous fluid, while below it the system is spinodally phase separated. (b) Ordering wavevectors corresponding to the phase boundary temperatures in (a).

typically not well removed from microdomain ordering scale, and rapidly varying (short-range) tail potentials that can modify local packing structure, features both absent in typical BCP liquids.

**A. Microphase Separation.** Figure 2 shows the spinodal microphase separation phase diagram and corresponding microdomain (ordering) wavevector,  $k^*$ , for *aabb* Janus rods with short-range square-well attractions ( $\alpha_b = 0.1\sigma$ ) and square-step repulsions ( $\alpha_a = 0.1\sigma$ ) at various repulsion-to-attraction strength ratios. Microphase spinodals are determined (for  $\phi > 0.05$ ) based on the most intense small angle peak, which here is  $S_{bb}(k)$ . As described in the previous section, the method of extrapolating the inverse value of the most intense peak of the static structure factor to determine a spinodal is found to be inaccurate for  $\phi < 0.05$ . We also limit our study to volume fractions below the random close packing (RCP) value of  $\phi \sim 0.55^{54}$  for hard rods of aspect ratio four.

Comparing the macrophase spinodal boundary of the purely attractive rods (filled symbols) with the microphase transition curves of the Janus rods (open symbols) in Figure 2, one sees that the macrophase transition is destroyed for Janus rods in the range  $0.05 < \phi < 0.55$ . Moreover, over most volume fractions, the Janus rod fluid must be cooled to lower temperatures to undergo microphase separation. The microphase separation (MiPS) temperature is also rather insensitive to the repulsion-to-attraction ratio at low to moderate volume fractions ( $\phi \leq 0.3$ ). We interpret this as a consequence of particles being too far apart to experience the short-range repulsion between the *a*-sites. At higher concentrations, however, the MiPS temperature increases strongly with volume fraction and is a nonmonotonic function of  $\epsilon_a/\epsilon_b$ , eventually saturating at  $\epsilon_a/\epsilon_b \approx 16$ . Microphase separation here is largely an attraction-driven clustering process given  $S_{bb}(k)$  has the

most intense microdomain-scale peak at low temperatures. This explains the initial reduction in the microphase ordering temperature with increasing repulsion-to-attraction strength ratio. However, the subsequent rise of the transition temperature as  $\epsilon_a/\epsilon_b > 1$  is more subtle. One might think the formation of tighter attractive contacts is even more favored when *a*–*a* repulsions are amplified, resulting in an extra driving force for attraction-driven ordering. However, this argument seems too naïve because this rise of the MiPS temperature at very high volume fractions is only found for square-step repulsions and not their Yukawa analog (see Section IV B), suggesting it is tied to the sharp cutoff of a square-step repulsive tail. The eventual saturation of the MiPS temperature is also a consequence of the square-step *a*–*a* repulsions because its sharp cutoff implies at large enough repulsive strengths a larger effective hard core diameter.

The corresponding ordering wavevector (here associated with  $S_{bb}(k)$ ) is shown in Figure 2b and defines the primary microdomain length scale as

$$L^* = \frac{2\pi}{k^*} \quad (7)$$

This periodicity varies from  $\sim 7.4\sigma$  to  $\sim 5.5\sigma$  as  $\phi$  increases, larger than a rod length, but smaller than twice it. It remains fairly independent of the repulsion-to-attraction strength ratio and is constant at high  $\phi$ . The gradual reduction with volume fraction of  $L^*$  indicates compaction of the microphase structure, but the underlying morphology is likely the same.

**B. Real Space Clustering and Self-Assembly.** The three site–site radial distribution functions corresponding to the system studied in the previous section are shown in Figure 3a at

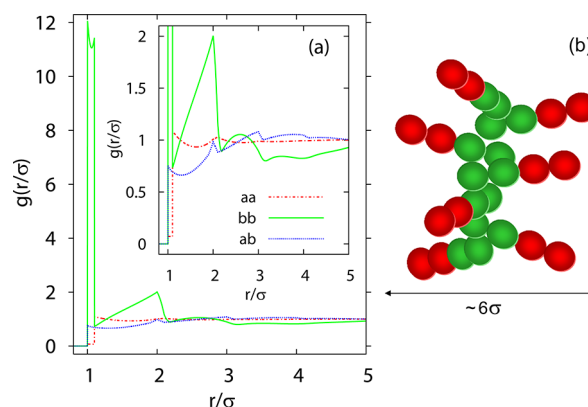


**Figure 3.** (a) Site–site radial distribution functions as a function of dimensionless intersite separation of a *aabb* Janus rod fluid with  $\alpha_a = \alpha_b = 0.1\sigma$ ,  $\phi = 0.21$ ,  $\epsilon_a/\epsilon_b = 1$ , and  $\epsilon_b = 2.75$ . (b) Schematic of the cylindrical micellar morphology expected for attraction-driven microphase separation.

$\phi = 0.21$  with  $\epsilon_a/\epsilon_b = 1$  at a temperature very close to the MiPS transition ( $T/\epsilon_b = 0.36$ ). These quantities provide information about the real space structure of the putative microphase ordered state as estimated from its highly correlated liquid state precursor. One sees a large amount of contact clustering between the attractive *b*-sites, and a depletion in *a*–*a* contacts within the range of tail repulsion. The inset compares the *bb* and *ab* components of the radial distribution function up to a separation of five site diameters. From these correlations, one sees that a *b*-site is likely to have many *b*-sites 1 and 2 site diameters away, whereas it preferentially has *a*-sites 3 and 4 site

diameters away. Figure 2b shows the microdomain length scale is  $\sim 6$  site diameters.

The combination of real space packing information and partial structure factors allows us to conjecture the microphase morphology in Figure 3b: a loosely ordered cylindrical micellar structure with the attractive  $b$ -sites in the center and repulsive  $a$ -sites on the periphery. Such an arrangement is stabilized largely by interparticle attractions. The radial distribution functions in Figure 3a are a representative example, and many low temperature calculations at other volume fractions suggest similarly ordered structures.

We quantify local clustering via the number of “bonded” nearest neighbors defined as the number of sites of type  $\nu$  that lie within a distance of the attractive range,  $\alpha_b$ , of a site of type  $\gamma$

$$nn_{\nu\gamma} = \rho_\nu \int_\sigma^{\sigma+\alpha_b} 4\pi r^2 g_{\nu\gamma}(r) dr \quad (8)$$

Figure 4a presents calculations of the number of sticky nearest  $b$ – $b$  neighbors in a  $aabb$  Janus rod fluid with  $\varepsilon_a/\varepsilon_b = 1$ , as a

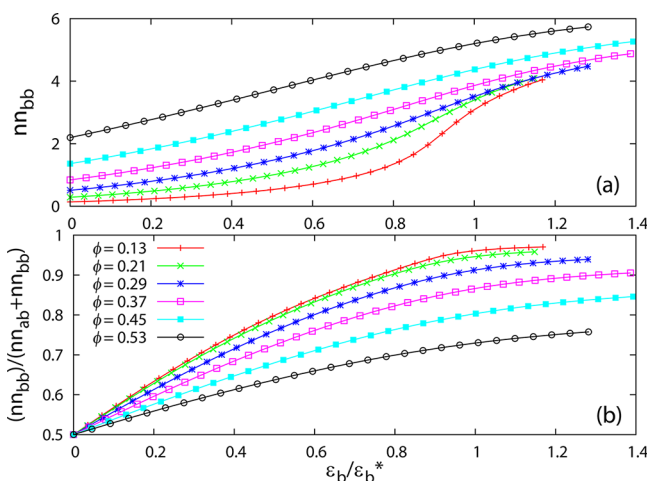


**Figure 4.** (a) Number of nearest  $b$ – $b$  neighbors within the range of attraction ( $\alpha_b$ ) as a function of the attraction strength (normalized by its spinodal microphase separation value) for a  $aabb$  Janus rod fluid with  $\alpha_a = \alpha_b = 0.1\sigma$  and  $\varepsilon_a/\varepsilon_b = 1$ . (b) The  $b$ – $b$  purity, that is, the fraction of the nearest neighbors of a  $b$ -site that are  $b$ -sites, for the same system as in (a).

function of the attraction strength normalized by its microphase separation value ( $\varepsilon_b^*$ ). Figure 5a shows the same quantity but in an “excess” representation where the “random” athermal contribution ( $nn_{bb}$  at  $\varepsilon_b = 0$ ) is subtracted. This excess number of  $b$ – $b$  neighbors ( $ex-nn_{bb}$ ) characterizes the degree of local cluster formation induced by the tail interactions.

Figure 4a shows that  $nn_{bb}$  saturates to similar values at low to intermediate volume fractions. By comparing Figures 4a and 5a, one sees that  $nn_{bb}$  and  $ex-nn_{bb}$  begin to saturate at attraction strengths slightly higher than the spinodal microphase transition temperature. Moreover, Figure 5a demonstrates a kind of “conservation law”:  $ex-nn_{bb} \sim 3$  for all  $\phi$  at the spinodal temperature, and this value of  $ex-nn_{bb}$  is conserved for all repulsion-to-attraction strength ratios studied. These trends suggest that the microphase separation (at the apparent spinodal level) or strong clustering temperature is determined by the formation of a critical number of sticky nearest neighbors rather than, say, the purity of the nearest neighbor shell. Support for this statement follows from Figure 4b, which

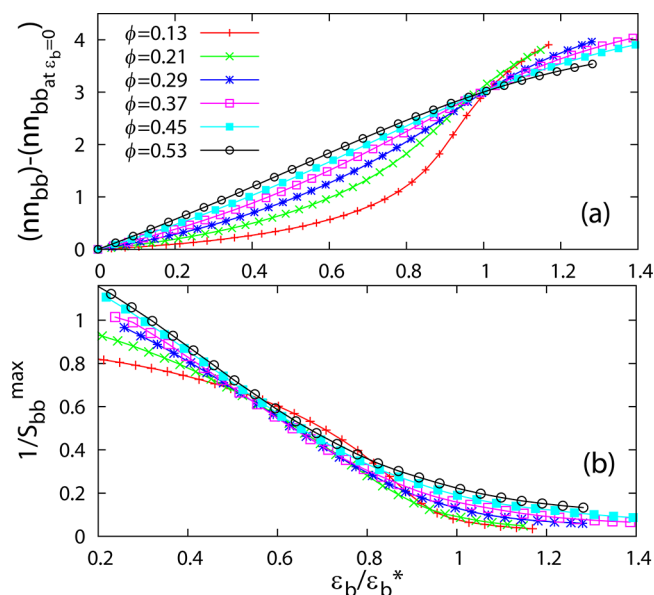


**Figure 5.** (a) “Excess” number of nearest  $b$ – $b$  neighbors within the range of attraction ( $\alpha_b$ ) as a function of attraction strength (normalized by its spinodal microphase separation value) for a  $aabb$  Janus rod fluid with  $\alpha_a = \alpha_b = 0.1\sigma$  and  $\varepsilon_a/\varepsilon_b = 1$ . (b) Inverse value of the fastest growing peak of the  $b$ – $b$  structure factor for the same system as in (a).

shows the fraction of nearest neighbor  $b$ -sites around a given  $b$ -site, a measure of the local purity of the clustered aggregate. The results suggest the microphase separation temperature is independent of purity. One also sees that the fraction of  $b$ -nearest neighbors around a  $b$ -site falls quickly with volume fraction, largely due to the fact that high  $\phi$  systems must satisfy excluded volume packing constraints at the cost of having more energetically favorable structures. Thus, the fraction of  $b$ -sites around a given  $b$ -site decreases with volume fraction even as the total number of  $b$ -sites increases (as is apparent from Figure 4b) in order to accommodate the large number of  $a$ -sites. The local compositional purity at high  $\phi$  decreases further with increasing repulsion-to-attraction strength ratios (e.g., at  $\varepsilon_a/\varepsilon_b = 4$ , figure not shown), because the  $a$ -sites are pushed away from each other more strongly and pack near  $b$ -sites, thereby introducing “defects” in the cylindrical micelle.

Recall that the microphase separation spinodal temperature is calculated by extrapolating to zero the inverse value of the fastest rising partial structure factor peak, and the behavior of this quantity ( $1/S_{bb}^{\max}$ ) is illustrated in Figure 5b. Comparing Figure 5a and b, one sees two interesting features. First, if the excess nearest neighbor curves are viewed in an inverted manner, their shapes are very similar to the  $1/S_{bb}^{\max}$  curves. This suggests that the rise in the number of nearest neighbors, a highly local real space structural quantity determined on the bead diameter length scale, is tightly correlated with the peak value of the structure factor, which is a Fourier space microdomain scale order parameter related to the overall size of the Janus rod. We find this connection to be nontrivial because the latter is a measure of the intensity of long (microdomain) wavelength oscillations of the pair correlation function is real space, a quantity distinct from the excess number of nearest neighbors. Second, the saturation of the number of nearest  $bb$  neighbors occurs at slightly higher attraction strengths than the saturation of the peak value of  $S_{bb}(k)$ .

The microdomain coherence length,  $\zeta$ , can be estimated from the inverse full-width at half-maximum of the structure factor peak feature,  $\Delta k_{1/2}$ , as  $\zeta = 2\pi/\Delta k_{1/2}$ . Figure 6a presents

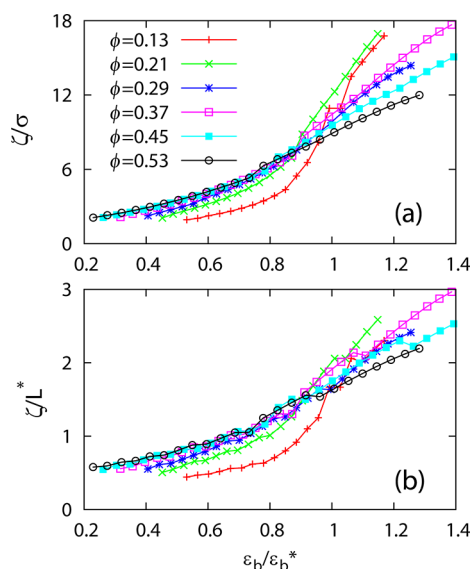


**Figure 6.** (a) Microdomain coherence length in units of the elementary site diameter as a function of attraction strength (normalized by its spinodal microphase separation value) for a *aabb* Janus rod fluid with  $\alpha_a = \alpha_b = 0.1\sigma$  and  $\varepsilon_a/\varepsilon_b = 1$ . (b) Coherence length in units of the microdomain ordering length scale.

calculations as the microphase transition is approached. The coherence length grows nearly exponentially at lower densities, but becomes an almost linear function of the normalized attraction strength at high volume fractions. Quantitatively, it lies between  $8\sigma$  and  $12\sigma$  at the spinodal temperature, and increases with further cooling. Figure 6b shows the coherence length attains the significant value of 2–3 microdomain periods.

#### IV. EFFECT OF ROD ASPECT RATIO AND INTERACTION POTENTIAL VARIATIONS

**A. Longer Janus Rods.** We now consider the effect of Janus rod aspect ratio on structure and phase behavior. Figure 7 shows microphase separation spinodal temperatures and ordering wavevectors for Janus rods of aspect ratio eight. These rods have a diblock, *aaaabbbb*, architecture with square-step (well) repulsion (attraction) of range  $\alpha_a = 0.1\sigma$  ( $\alpha_b = 0.1\sigma$ ). The phase diagram is only calculated up to  $\phi = 0.45$ , slightly below the estimated RCP volume fraction for these longer rods.<sup>54</sup> One sees the microphase ordering temperature is almost 1.5 times the value for *aabb* rods, indicating the expected easier microphase separation. However, the overall features and shape of the microphase separation curves remain largely similar to the *aabb* Janus rods. As with the latter, the lower volume fraction ( $\phi \leq 0.3$ ) ordering temperature is fairly insensitive to the repulsion-to-attraction strength ratio and volume fraction, whereas the high  $\phi$  MiPS temperature is a nonmonotonic function of the repulsion-to-attraction ratio. Figure 7b demonstrates that the ordering length scales vary from  $\sim 11\sigma$  at low volume fractions to  $\sim 8.5\sigma$  at high  $\phi$ . These values are only  $\sim 1.5$ – $1.6$  times that of the 4-site Janus rod analogs. Both the  $k^*$  values, and radial distribution functions (not shown),

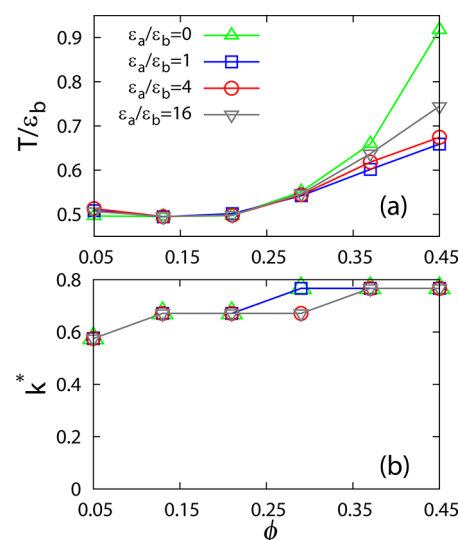


**Figure 7.** (a) Microphase separation spinodal temperatures of a fluid of 8-site Janus rods of *aaaabbbb* diblock architecture with  $\alpha_a = \alpha_b = 0.1\sigma$ . (b) Ordering wavevectors corresponding to the microphase separation temperatures in (a).

suggest a cylindrical micellar morphology similar to the *aabb* system, as discussed in section III.

**B. Effect of Interparticle Tail Potentials.** Many studies of homogeneous sticky spherical particles have revealed that the form and range of beyond-hard-core tail potential(s) can be of decisive importance in determining phase behavior.<sup>24,55,56</sup> In this subsection, we explore the structure and phase behavior of Janus rods as the range and functional form of interaction potential is changed.

Figure 8 illustrates the consequences of greatly increasing the range of the repulsive tail potential from 10 to 50% the site diameter ( $\alpha_a = 0.5\sigma$ ) holding the attraction range fixed at  $\alpha_b = 0.1\sigma$ . The longer range repulsive tail introduces strongly nonadditive packing (entropic) effects. The ordering length scale at high  $\phi$  shown in Figure 8b occurs at  $k^*\sigma \sim 5$ , roughly

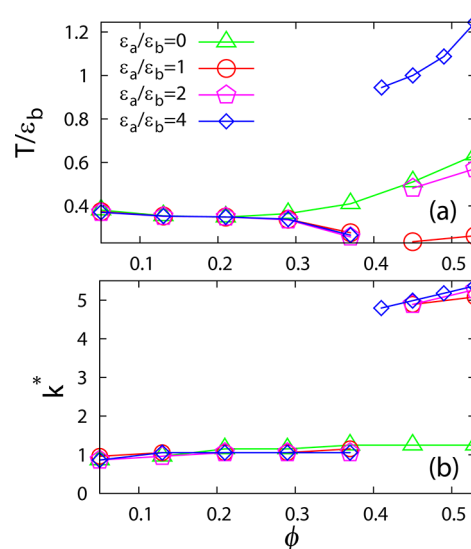


**Figure 8.** (a) Microphase separation temperatures of a fluid of 4-site Janus rods of *aabb* architecture with  $\alpha_a = 0.5\sigma$  and  $\alpha_b = 0.1\sigma$ . (b) Ordering wavevectors corresponding to the microphase separation temperatures in (a).

corresponding to the diameter of a site plus repulsion range. Upon cooling, the most rapidly growing partial structure factor is  $S_{aa}(k)$ , suggesting repulsion-driven microphase ordering. This contrasts with the behavior at lower volume fraction where  $S_{bb}(k)$  is the most intense partial structure factor, indicating attraction-driven ordering on the rod length scale.

Figure 9 shows an example of the  $a$ - $a$  and  $b$ - $b$  partial structure factors for this system at  $\phi = 0.45$ ,  $\varepsilon_a/\varepsilon_b = 4$ , and  $\varepsilon_b =$

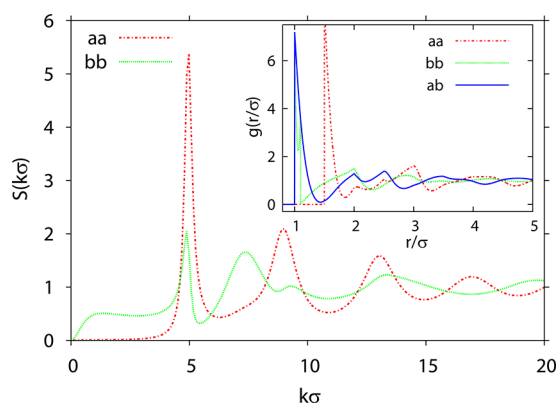


**Figure 9.** Partial structure factors ( $a$ - $a$  and  $b$ - $b$ ) for a fluid of  $aabb$  Janus rods with  $\alpha_a = 0.5\sigma$ ,  $\alpha_b = 0.1\sigma$ ,  $\phi = 0.45$ ,  $\varepsilon_a/\varepsilon_b = 4$ , and  $\varepsilon_b = 4$ . The inset shows the  $a$ - $a$ ,  $b$ - $b$ , and  $a$ - $b$  site-site radial distribution functions of the same system.

4. One sees that  $S_{aa}(k)$  has a larger peak (on the  $k^*\sigma \sim 5$  length scale) in this region. This feature, along with the fact that the large growth of intensity at these larger wavevectors only occurs at high repulsion range and for large repulsion-to-attraction ratios, clearly indicates assembly at high volume fractions is repulsion-driven. This deduction is further supported by the radial distribution functions immediately above the high density transition temperatures (inset of Figure 9) which have large peaks on the  $\sigma + \alpha_a$  length scale. We henceforth call this high  $\phi$ , repulsion-driven branch of the phase diagram the “MiPS-2 (Microphase Separation-2)” region, and the lower  $\phi$  branch in Figure 8a that corresponds to ordering on the  $\sim 7.4\sigma$ - $5.5\sigma$  rod length scale the “MiPS-1” region.

The MiPS-2 temperatures in Figure 8a are determined from the peak value of the  $a$ - $a$  structure factor, while MiPS-1 temperatures from the peak of  $S_{bb}(k)$ . As found for the short-range repulsion ( $\alpha_a = 0.1\sigma$ ) Janus rods, an  $\varepsilon_a/\varepsilon_b$ -independent behavior of the MiPS-1 temperature occurs in the lower volume fraction regime. However, due to the longer repulsive range, the MiPS-1 temperature begins to become sensitive to the repulsion-to-attraction strength ratio at lower volume fractions than for the  $\alpha_a = 0.1\sigma$  system. At high  $\phi$ , the attraction driven MiPS-1 state is destroyed and is replaced by the repulsion driven MiPS-2 state. The MiPS-2 temperature rises with increasing  $\varepsilon_a/\varepsilon_b$  indicating easier ordering as  $a$ -sites become more repulsive. There is a gap between the fluid, MiPS-1, and MiPS-2 regions of the phase diagram. It is unclear based on our extrapolated spinodal analysis whether this suggests a triple point, or the fluid region extends to zero temperature. It is also possible that a different kind of phase exists such as in block copolymers.<sup>57</sup>

Increasing the repulsion range to  $\alpha_a = 0.5\sigma$  results in sufficient steric frustration at high concentration to disrupt the micellar MiPS-1 structure and impose a spatial organization that minimizes  $a$ - $a$  contacts (Figure 9 inset). Specifically, the

Janus rods largely give up the energetically favorable  $b$ - $b$  contacts in favor of  $a$ - $b$  contacts. This behavior is quantified in Figure 10, which plots the  $b$ -purity of the nearest neighbor shell

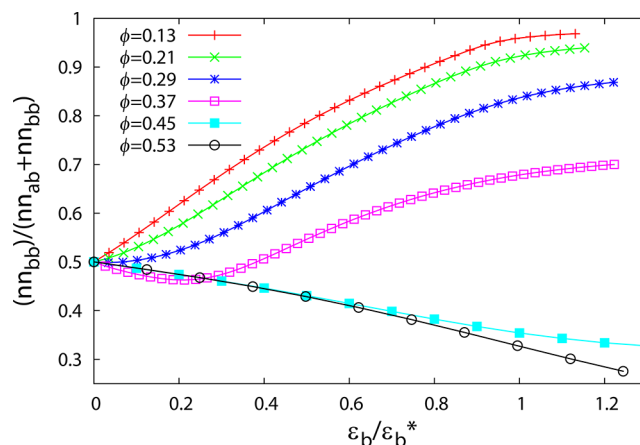


**Figure 10.** The  $b$ - $b$  purity, that is, the fraction of the nearest neighbors of a  $b$ -site that are also  $b$ -sites, as a function of the attraction strength (normalized by its spinodal microphase value) for a fluid of  $aabb$  Janus rods with  $\alpha_a = 0.5\sigma$ ,  $\alpha_b = 0.1\sigma$ , and  $\varepsilon_a/\varepsilon_b = 4$ .

of a  $b$ -site (where a nearest neighbor is defined as a site lying within the attractive range of a  $b$ -site), as a function of the attraction strength normalized by its microphase spinodal value. One sees here that  $b$ - $b$  contacts are dominant at volume fractions where we expect attraction-driven micellar structures (the MiPS-1 region,  $k^*\sigma \sim 1$ ). At high  $\phi$  (where  $k^*\sigma \sim 5$ ), the fraction of  $b$ - $b$  contacts decreases, resulting in a larger fraction of  $a$ - $b$  contacts. Indeed, the fraction of  $b$ - $b$  contacts decreases as a function of the attraction strength in the high volume fraction MiPS-2 regime as a result of a corresponding increase in the repulsive strength at a constant  $\varepsilon_a/\varepsilon_b = 4$ . This occurs because the longer range  $b$ - $b$  repulsion pushes  $a$ -sites closer to  $b$ -sites at the cost of attractive interactions between  $b$ -sites. Figure 10 also demonstrates a dramatic difference in the preference for  $b$ - $b$  contacts versus  $a$ - $b$  contacts as the Janus particle concentration increases from the attraction-driven MiPS-1 region to the repulsion-driven MiPS-2 region and the corresponding disruption of the micellar clusters. The origin of this behavior is in the large  $ab$  peak of the radial distribution function as compared to the  $bb$  peak (as seen in the inset of Figure 9).

Figure 11a shows that the number of nearest  $b$ - $b$  neighbors grows and then saturates in systems that form micellar-like structures. On the other hand, at higher  $\phi$ , the number of nearest  $b$ - $b$  neighbors either decrease or remain constant. Note that  $\phi = 0.37$  is very close to the transition between the two kinds of microphase ordered structures (see Figure 8) and, hence, exhibits slightly different behavior than the rest of the MiPS-1 systems. The differences between the lower concentration micellar and the repulsion dominated high volume fraction structures is most vividly illustrated by Figure 11b. For micelles, the excess number of  $b$ - $b$  neighbors is  $\sim 3$  at the microphase separation temperature (as also found for the  $\alpha_a = 0.1\sigma$  system), while it is either negative or nearly zero for high density structures.

We now consider the opposite mismatched tail potential system, that is, a long-range attraction of  $\alpha_b = 0.5\sigma$  and short-range repulsion of  $\alpha_a = 0.1\sigma$ . The results in Figure 12a show



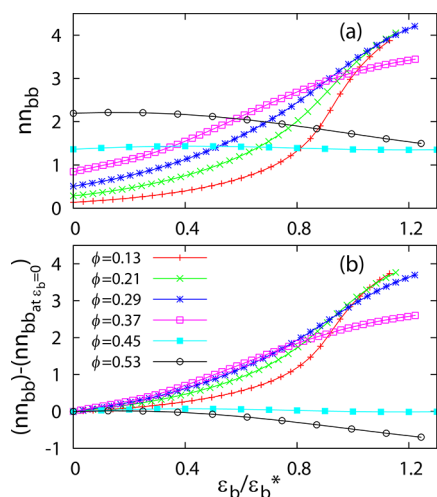


**Figure 11.** (a) Number of nearest  $b$ - $b$  neighbors within the range of attraction ( $\alpha_b$ ) as a function of the attraction strength (normalized by its spinodal transition value) for a fluid of  $aabb$  Janus rods with  $\alpha_a = 0.5\sigma$ ,  $\alpha_b = 0.1\sigma$ , and  $\epsilon_a/\epsilon_b = 4$ . (b) The "excess" number of nearest  $b$ - $b$  neighbors within the range of attraction.

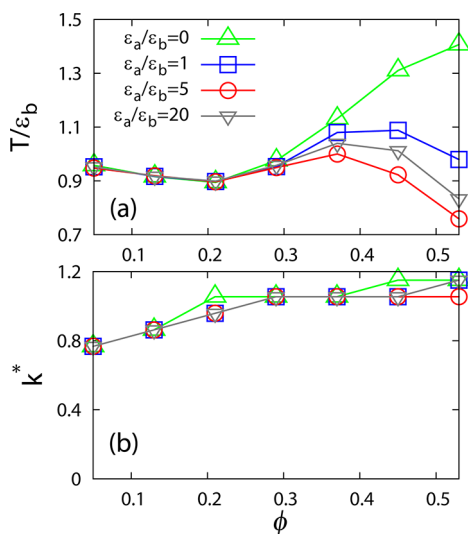


**Figure 12.** (a) Microphase separation temperatures as a function of volume fraction of a fluid of  $aabb$  Janus rods with  $\alpha_a = 0.1\sigma$  and  $\alpha_b = 0.5\sigma$ . (b) Ordering wavevectors corresponding to the microphase separation temperatures in (a).

that the MiPS-1 state is preserved at high volume fractions and a nearly 2.5-fold increase in the MiPS-1 transition temperature because this transition is attraction driven. One also sees a nonmonotonic variation of the spinodal temperature with volume fraction at high  $\phi$ , in qualitative contrast to the  $\alpha_a = \alpha_b = 0.1\sigma$  system (Figure 2). However, much like the latter, Figure 12a shows a nonmonotonic dependence of the transition temperature on the repulsion-to-attraction strength ratio. Additionally, Figure 12b indicates that the length scale and morphology of the microphase ordered state does not change as the attractive range increases. We emphasize that, while increasing the repulsive range results in a new microphase morphology, changing the attraction range only modifies the spinodal temperature.

It seems remarkable that no macrophase separation is predicted for such a large attraction range, even when  $\epsilon_a/\epsilon_b = 0$ .

This behavior contrasts with simulation studies of Janus<sup>11</sup> and other patchy<sup>58</sup> spheres, where liquid–gas transitions occur at such attraction ranges. We note that our prior RISM-RPA calculations<sup>26</sup> for Janus spheres with  $\alpha_b = 0.5\sigma$  and  $\epsilon_a/\epsilon_b = 0$  did find macrophase separation up to  $\phi = 0.13$ . Hence, Janus rods display a stronger preference for microphase ordering relative to macrophase separation than their sphere analog.

So far, we have used square-well attractions and square-step repulsions as minimalist models for hydrophobic attractions and Coulombic repulsions, respectively, as commonly done in the very limited simulations performed to date. However, square-step repulsions are obviously not a quantitatively accurate description of charge repulsions. Hence, we briefly investigate the phase behavior of Janus rods with short-range ( $\alpha_b = 0.1\sigma$ ) square-well attractions and longer range ( $\alpha_a = 0.5\sigma$ ) Yukawa repulsions using

$$U_{aa}(r) = \infty, \quad r \leq \sigma$$

$$U_{aa}(r) = \frac{\epsilon_a}{r/\sigma} e^{-(r-\sigma)/\alpha_a}, \quad r > \sigma \quad (9)$$

Figure 13 presents the spinodal temperatures and ordering wavevectors for this 4-site Janus rod system. As found for the

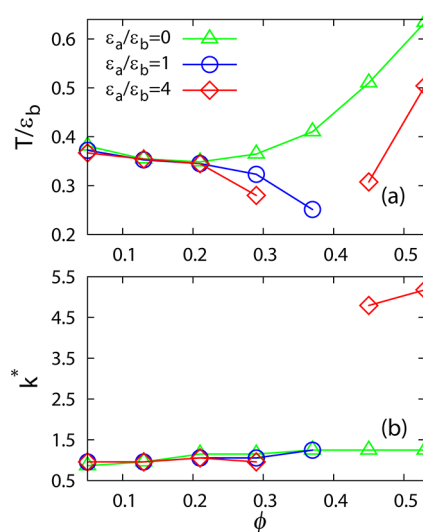


**Figure 13.** (a) Microphase separation temperatures as a function of volume fraction of a fluid of  $aabb$  Janus rods with a repulsive Yukawa potential between  $a$ -sites of range  $\alpha_a = 0.5\sigma$ , and square-well attractions between  $b$ -sites of range  $\alpha_b = 0.1\sigma$ . (b) Ordering wavevectors corresponding to the microphase separation temperatures in (a).

square-well plus square-step system, the MiPS-1 temperature is unaffected by the repulsion-to-attraction strength ratio at lower  $\phi$ . However, these attraction-driven microphase transition temperatures do decrease with  $\epsilon_a/\epsilon_b$  starting at a comparatively lower  $\phi$  due to the longer range repulsions. Moreover, they do not display the nonmonotonic behavior found for the  $\alpha_a = 0.5\sigma$  square well repulsive systems. At higher  $\phi$ , the square-well–Yukawa system does undergo a repulsion-driven MiPS-2 phase transition with the fastest rising partial structure factor being  $S_{aa}(k)$ .

Because the repulsive Yukawa interaction between  $a$ -sites decays rather slowly compared to the square step potential, the transition from the MiPS-1 ( $k^* \sim 1$ ) to MiPS-2 ( $k^*\sigma \sim 5$ ) ordered state with increasing  $\epsilon_a/\epsilon_b$  is slower than seen in Figure



9. However, what occurs in the region of the phase diagram between the attraction and repulsion driven microphase separation transitions is again unclear. Overall, we conclude that using a more realistic potential to model Coulombic repulsions seems to result mainly in only quantitative differences in phase behavior.

## V. RISM-RPA APPROACH

As discussed in the Introduction, the coarse-grained incompressible RPA approach is popular in the study of self-assembling polymeric systems where there is a wide separation between the local monomer and microdomain ordering length scales.<sup>44,49,59,60</sup> Intermolecular correlations between polymer chains are discarded in the simplest mean field approximation. In this section, we briefly discuss the extension to Janus rods of our previously proposed (for Janus spheres) compressible RISM-RPA approach.<sup>26</sup> This simplified hybrid theory properly enforces interparticle excluded volume constraints *only* in the absence of tail potentials, with the latter crudely treated in a perturbative mean field spirit.<sup>26</sup> Tail-potentials drive microphase separation, but their consequences on, and coupling to, local correlations and the core exclusion constraint are ignored. As a consequence, a literal microphase spinodal ( $S_{ij}(k^*) \rightarrow \infty$ ) is predicted, as in the Leibler theory of block copolymers.<sup>49</sup> The technical simplifications based on this approximation merit its study as a possibly useful and easy to implement zeroth order approach for Janus rod assembly.

**A. Theory.** One first needs to solve a single RISM equation in the athermal limit for a hard rod. The required Fourier-space intramolecular distribution function is

$$\begin{aligned}\Omega(k) &= \rho\omega(k) = \rho \sum_{\nu,\gamma=1}^N \omega_{\nu\gamma}(k) \\ &= \rho \left( 4 + 6 \frac{\sin k\sigma}{k\sigma} + 4 \frac{\sin 2k\sigma}{2k\sigma} + 2 \frac{\sin 3k\sigma}{3k\sigma} \right)\end{aligned}\quad (10)$$

To restore the chemical asymmetry between the *a*- and *b*-sites, a mean field random phase approximation (RPA) is employed corresponding to the additive approximation:

$$C_{MM'}(k) = C_{MM'}^0(k) + \Delta C_{MM'}(k) \quad (11)$$

where  $C_{MM'}^0(k) = C^0(k)$  is the Fourier transform of the direct correlation function for all *M* and *M'* in the athermal limit (neglecting end effects), and  $\Delta C_{MM'}(k)$  is the correction due to tail potentials:

$$\begin{aligned}\Delta C_{MM'}(r) &= 0, \quad r \leq \sigma \\ \Delta C_{MM'}(r) &= -\beta U_{MM'}(r), \quad r > \sigma\end{aligned}\quad (12)$$

Each element in the matrix of collective partial structure factors in eq 2 has a common denominator,  $\Lambda = \det \mathbf{I} - \Omega(k)\mathbf{C}(k)$ . The RISM-RPA method locates a microphase spinodal transition by determining the temperature and ordering wavevector,  $k^*$ , at which the all partial structure factors simultaneously first diverge corresponding to the condition

$$\begin{aligned}\Lambda(k^*) &= 0 = 1 - \rho\omega_{aa}(k^*)C_{aa}(k^*) - \rho\omega_{bb}(k^*)C_{bb}(k^*) \\ &\quad - 2\rho\omega_{ab}(k^*)C_{ab}(k^*) + \rho^2[\omega_{aa}(k^*)\omega_{bb}(k^*) \\ &\quad - \omega_{ab}^2(k^*)][C_{aa}(k^*)C_{bb}(k^*) - C_{ab}^2(k^*)]\end{aligned}\quad (13)$$

If  $k^* = 0$ , the divergence indicates macrophase separation, whereas  $k^* \neq 0$  indicates microphase separation. Combining eqs 11–13 yields a quasi-analytic spinodal condition:

$$\begin{aligned}\frac{P(k)}{Y^2(k, \alpha_b)} \left( \frac{T}{\varepsilon_b} \right)^2 + \left[ \frac{R(k)Y(k, \alpha_a)}{Y(k, \alpha_b)} \left( \frac{\varepsilon_a}{\varepsilon_b} \right) - E(k) \right] \frac{1}{Y(k, \alpha_b)} \\ \left( \frac{T}{\varepsilon_b} \right) - \frac{F(k)Y(k, \alpha_a)}{Y(k, \alpha_b)} \left( \frac{\varepsilon_a}{\varepsilon_b} \right) = 0\end{aligned}\quad (14)$$

$$P(k) = 1 - \rho C^0(k)(\omega_{aa}(k) + \omega_{bb}(k) - 2\omega_{ab}(k))$$

$$R(k) = \rho[\rho C^0(k)(\omega_{aa}(k)\omega_{bb}(k) - \omega_{ab}^2(k)) - \omega_{aa}(k)]$$

$$E(k) = \rho[\rho C^0(k)(\omega_{aa}(k)\omega_{bb}(k) - \omega_{ab}^2(k)) - \omega_{bb}(k)]$$

$$F(k) = \rho^2(\omega_{aa}(k)\omega_{bb}(k) - \omega_{ab}^2(k))$$

$$\begin{aligned}Y(k, \alpha) &= \frac{4\pi}{k^3} [k\sigma \cos(k\sigma) - k(\sigma + \alpha) \cos(k(\sigma + \alpha)) \\ &\quad + \sin(k(\sigma + \alpha)) - \sin(k\sigma)]\end{aligned}$$

In practice, eq 14 is solved for a hypothetical spinodal temperature as a function of wavevector. The physical behavior is then identified as the first instability occurring at a wavevector  $k^*$  associated with the maximum spinodal temperature.

**B. Results.** We now present a few representative RISM-RPA phase diagrams and contrast the results with the RISM theory analogs discussed in sections III and IV. Recall that the ordering wavevector of Janus rods with  $\alpha_a = \alpha_b = 0.1\sigma$  shows no sudden changes based on the RISM theory (Figure 2b). This is in sharp contrast to the behavior predicted by RISM-RPA in Figure 14b. At low repulsion-to-attraction strength ratios, the ordering wavevectors are the same for both theories. But at higher repulsion-to-attraction strength ratios, spinodal microphase divergences on two additional length scales are found in RISM-RPA: the site scale ( $\sim\sigma$ ), which can be interpreted as

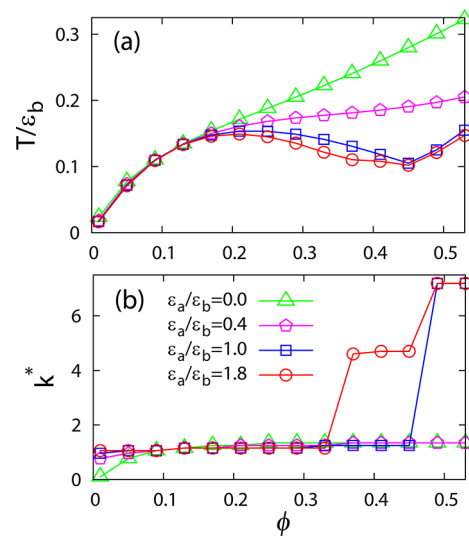


**Figure 14.** Hybrid RISM-RPA theory calculations. (a) Spinodal temperatures as a function of volume fraction of a fluid of Janus rods of *aabb* architecture with  $\alpha_a = \alpha_b = 0.1\sigma$ . (b) Wavevectors of divergent structure factors at the mean field microphase spinodal transition corresponding to the temperatures in (a).

site-level crystallization, and a length scale slightly larger. The former is only found at very high  $\phi$ , while the latter is only present at large repulsion-to-attraction strength ratios. Specifically, as the latter ratio increases beyond roughly unity, the RPA-based theory predicts a transition at  $k^*\sigma \sim 5$ . This seems to be the analog of the MiPS-2 ordering transition of RISM theory found at higher  $\varepsilon_a/\varepsilon_b$  (see Figures 8 and 13). However, RISM only predicts a MiPS-2 phase at larger repulsive ranges. Thus, the RPA simplification results in greater sensitivity of phase behavior to variations in the interparticle potential.

The appearance of the above two different microdomain order length scales is one of the main differences between RISM and its RPA-based analog. Comparison of Figures 2 and 14 also shows MiPS temperatures are significantly lower in the RISM-RPA approach. In accord with RISM results, the RPA version does predict  $\varepsilon_a/\varepsilon_b$  independent transition temperatures in the lower  $\phi$  regime. On the other hand, the shape of the microphase phase boundaries as a function of volume fraction are qualitatively different, which is the second major difference between the two theories. Recall RISM theory predicts the MiPS temperature is fairly constant at  $\phi \leq 0.3$ , whereas RISM-RPA finds it increases with  $\phi$  in this regime. In the high density regime, the MiPS temperature decreases with volume fraction.

At  $\phi = 0.01$  and  $\varepsilon_a/\varepsilon_b = 0$ , RISM-RPA theory predicts macrophase separation ( $k^* = 0$ ). This cannot be probed by RISM theory because the extrapolation procedure is not reliable at such low volume fractions. Moreover, the site-level spinodal crystallization predicted by RISM-RPA cannot rigorously be analyzed within RISM theory. Figure 15 shows

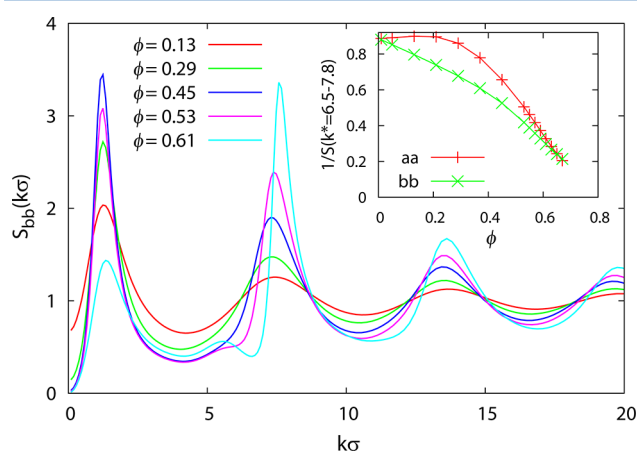


**Figure 15.** Full RISM theory calculations of the  $b$ – $b$  partial structure factor of an  $aabb$  Janus rod system with  $\alpha_a = \alpha_b = 0.1\sigma$ ,  $\varepsilon_a/\varepsilon_b = 4$ , and  $\varepsilon_b = 2$ . The inset shows the inverse value of the primary peak of the  $a$ – $a$  and  $b$ – $b$  partial structure factors.

structure factors of the latter up to very high volume fractions. Of course there are no divergences, but if one speculatively invokes the Verlet–Hansen “rule”<sup>44</sup> that crystallization occurs when the peak reaches  $\sim 2.85$ , then crystallization occurs at  $\phi \sim 0.56$ . So far we have avoided performing calculations beyond  $\phi \sim 0.55$ , which is the RCP volume fraction of hard rods of aspect ratio four. However, because site level crystallization necessarily occurs at high densities, for illustrative purposes, Figure 15 demonstrates the dominance of the primary (site length scale) peak as the volume fraction exceeds 0.55. The inset plots the inverse value of the primary peak of the  $a$ – $a$  and  $b$ – $b$  static structure factors. One sees a rapid increase of the primary peak

intensity beyond  $\phi = 0.55$ , and a shift in intensity from the microphase ordering wavevector ( $k^* \sim 1$ ) to the primary peak.

Based on our limited studies, we conclude that the RISM-RPA approach seems capable of capturing the type of phase behaviors predicted by RISM theory, albeit not at the same system conditions and with significant quantitative differences. It also predicts effects not present in RISM theory, which are presumably destroyed by many body correlation effects that the RPA ignores. Nevertheless, RISM-RPA might be a useful tool to quickly explore possible microphase ordering transitions, and suggest promising systems to study using the more computationally intensive RISM theory or much more computationally demanding computer simulation.

## VI. SUMMARY AND DISCUSSION

We have applied RISM integral equation theory to perform the first study of the structure and phase behavior of relatively short diblock Janus rods which are attractive on one end and repulsive on the other. An attraction-driven microphase separation (MiPS-1) is predicted for short attraction and repulsion ranges ( $\alpha_a = \alpha_b = 0.1\sigma$ ). Educated conjectures for real space aggregate structure can be made based on knowledge of the three site–site radial distribution functions and the partial structure factors. The rods appear to assemble into a micellar cylinder with attractive sites in the interior and repulsive sites on the outside. The transition temperature grows as the attractive range and rod length increase. At lower rod volume fractions, the microphase spinodal temperature is nearly independent of concentration and the attraction-to-repulsion strength ratio, because the relatively longer intermicelle distances prevent the rods from experiencing the short-range repulsive tail potentials. On the other hand, the high volume fraction branch of the phase diagram shows a nonmonotonic dependence of the MiPS-1 transition temperature on the repulsion-to-attraction ratio.

If the tail repulsion range between  $a$ -sites is increased to  $\alpha_a = 0.5\sigma$ , then in the high volume fraction regime the attraction driven MiPS-1 ordered state is destroyed. Here, the outward facing repulsive sites on the cylindrical micelles come within their mutual repulsion range, and the system gives up attractive  $b$ – $b$  contacts interactions in order to avoid repulsive  $a$ – $a$  contacts. This results in the dissolution of the MiPS-1 micellar morphology in favor of a different repulsion-driven MiPS-2 state of organization. A new ordering wavevector emerges corresponding to the net repulsive interaction range of  $a$ -sites ( $\sigma + \alpha_a$ ), and the fastest growing structure factor peak with cooling changes to  $S_{aa}(k)$ . Based on an analysis of both the Fourier space partial structure factors and the three real space site–site radial distribution functions, we deduce that the MiPS-2 transition is fundamentally determined not by cohesive interparticle contacts, but rather from a shorter wavelength periodic arrangement associated with a distance of avoidance between  $a$ -sites which determines the  $b$ -site spatial organization. This repulsion-driven microphase separation occurs at higher temperatures as the repulsion-to-attraction strength ratio grows.

The excess number of nearest  $b$ – $b$  neighbors is a local measure of aggregate structure. Interestingly, it is found to be tightly correlated to  $S_{bb}^{\max}$ , a global (Janus rod length) measure of microdomain order. Furthermore, the former quantity appears to be a distinctive indicator of microphase separation and microdomain spatial coherence because it tends to saturate just below the MiPS-1 transition temperature and at the spinodal

temperature, it attains a value of  $\sim 3$  for all volume fractions, repulsion-to-attraction ratios, and ranges of repulsion studied. In qualitative contrast, it either decreases, or remains constant, as a function of the attraction strength, in the repulsion-dominated MiPS-2 region.

Liquid–gas macrophase separation in the Janus rod systems is absent, even when the attractive range is as large as  $\alpha_b = 0.5\sigma$ , for volume fractions  $\phi \geq 0.05$ , in contrast to the behavior of Janus spheres.<sup>11,26,58</sup> Hence, it appears the introduction of shape anisotropy provides additional suppression of macrophase separation.

We find that the much simpler RISM-RPA hybrid approach can reproduce the global microcosm of possible Janus rod phase behaviors found based on the RISM theory. Although the shape of the microphase spinodal curves are different from those determined by the full RISM calculation, the behavior of the ordering wavevector is similar. Overall, the mean field RISM-RPA approach predicts phase diagrams that are more sensitive to small changes in system parameters, presumably a reflection of the neglect of disordered phase stabilizing fluctuations, though trends are usually qualitatively correct.

Of course, the accuracy of the RISM theory predictions are not a priori known. What is required are new computationally intensive computer simulations of Janus rod models to test our results for the real and Fourier space structure in the homogeneous fluid and also the estimated phase boundaries. Confocal microscopy and small angle scattering experiments are also highly desirable to test the theory. We hope our present theoretical results motivate efforts along these lines.

Finally, the RISM approach can be extended to Janus rods of other compositions and architectures (AB sequences), non-matched elementary site diameters, and nonuniaxial objects. The availability of real and Fourier space pair correlations can serve as input to microscopic dynamical theories of kinetic arrest (glasses, gels), activated relaxation, and rheology.<sup>61–65</sup> The ability to predict pair correlations at short distances (“contacts”) and to a lesser extent the microdomain coherence length in a globally amorphous but segregated material would seem to be especially important in applications where charge, ions, or energy is transported via very short-range exchange processes.

## AUTHOR INFORMATION

### Corresponding Author

\*E-mail: kschweiz@illinois.edu.

### Present Address

<sup>†</sup>Indian Institute of Technology Bombay, Mumbai, India.

### Notes

The authors declare no competing financial interest.

## ACKNOWLEDGMENTS

We thank Steve Granick and Jennifer Lewis for stimulating and informative discussions of their experiments on Janus spheres and rods which motivated this research. The work was supported by DOE-BES under Grant No. DE-FG02-07ER46471 via the Frederick Seitz Materials Research Laboratory.

## REFERENCES

- (1) Nisisako, T.; Torii, T.; Takahashi, T.; Takizawa, Y. *Adv. Mater.* **2006**, *18*, 1152–1156.
- (2) Roh, K.-ho; Martin, D. C.; Lahann, J. *Nat. Mater.* **2005**, *4*, 759–63.
- (3) Jiang, S.; Schultz, M. J.; Chen, Q.; Moore, J. S.; Granick, S. *Langmuir* **2008**, *24*, 10073–10077.
- (4) Jiang, S.; Granick, S. *Langmuir* **2008**, *24*, 2438–2445.
- (5) Pawar, A. B.; Kretzschmar, I. *Langmuir* **2008**, *24*, 355–358.
- (6) He, J.; Hourwitz, M. J.; Liu, Y.; Perez, M. T.; Nie, Z. *Chem. Commun.* **2011**, *47*, 12450–2.
- (7) Anthony, S. M.; Kim, M.; Granick, S. *Langmuir* **2008**, *24*, 6557–6561.
- (8) Hong, L.; Cacciuto, A.; Luijten, E.; Granick, S. *Langmuir* **2008**, *24*, 621–5.
- (9) Fantoni, R. *Eur. Phys. J. B* **2012**, *85*, 108.
- (10) Rosenthal, G.; Klapp, S. H. L. *J. Chem. Phys.* **2011**, *134*, 154707.
- (11) Sciortino, F.; Giacometti, A.; Pastore, G. *Phys. Rev. Lett.* **2009**, *103*, 1–4.
- (12) Rosenthal, G.; Gubbins, K. E.; Klapp, S. H. L. *J. Chem. Phys.* **2012**, *136*, 174901.
- (13) de Gennes, P.-G. *Rev. Mod. Phys.* **1992**, *64*, 645–648.
- (14) Song, J. H. K.; Kretzschmar, I. *ACS Appl. Mater. Interfaces* **2009**, *1*, 1747–1754.
- (15) Howse, J. R.; Jones, R. A. L.; Ryan, A. J.; Gough, T.; Vafabakhsh, R.; Golestanian, R. *Phys. Rev. Lett.* **2007**, *99*, 048102.
- (16) Wheat, P. M.; Marine, N. A.; Moran, J. L.; Posner, J. D. *Langmuir* **2010**, *26*, 13052–13055.
- (17) Choi, J.; Zhao, Y.; Zhang, D.; Chien, S.; Lo, Y.-H. *Nano Lett.* **2003**, *3*, 995–1000.
- (18) Behrend, C. J.; Anker, J. N.; Kopelman, R. *Appl. Phys. Lett.* **2004**, *84*, 154.
- (19) Sakurai, S.; Kawada, H.; Hashimoto, T.; Fetters, L. J. *Macromolecules* **1993**, *26*, 5796–5802.
- (20) Matsen, M. W.; Schick, M. *Phys. Rev. Lett.* **1994**, *72*, 2660–2663.
- (21) Angerman, H. J.; Ten Brinke, G. *Eur. Phys. J. E* **2003**, *10*, 337–343.
- (22) Neumann, C.; Loveday, D. R.; Abetz, V.; Stadler, R. *Macromolecules* **1998**, *31*, 2493–2500.
- (23) Lodge, T. P.; Pudil, B.; Hanley, K. J. *Macromolecules* **2002**, *35*, 4707–4717.
- (24) Sear, R. P.; Gelbart, W. M. *J. Chem. Phys.* **1999**, *110*, 4582.
- (25) Sear, R. P.; Chung, S. W.; Markovich, G.; Gelbart, W. M.; Heath, J. R. *Phys. Rev. E* **1999**, *59*, R6255–8.
- (26) Jiang, S.; Chen, Q.; Tripathy, M.; Luijten, E.; Schweizer, K. S.; Granick, S. *Adv. Mater.* **2010**, *22*, 1060–1071.
- (27) Chen, Q.; Bae, S. C.; Granick, S. *Nature* **2011**, *469*, 381–4.
- (28) Chen, Q.; Diesel, E.; Whitmer, J. K.; Bae, S. C.; Luijten, E.; Granick, S. *J. Phys. Chem. B* **2011**, *113*, 7725–7727.
- (29) Romano, F.; Sciortino, F. *Soft Matter* **2011**, *7*, 5799.
- (30) Chen, Q.; Bae, S. C.; Granick, S. *J. Am. Chem. Soc.* **2012**, *134*, 11080–11083.
- (31) Shaviv, E.; Schubert, O.; Alves-Santos, M.; Goldoni, G.; Di Felice, R.; Vallee, F.; Fatti, N. D.; Banin, U.; Sonnichsen, C. *ACS Nano* **2011**, *5*, 4712–4719.
- (32) Deconinck, A. J. Fabrication, dynamics and self-assembly of anisotropic colloidal particles. *M.S. Thesis*, University of Illinois, Urbana–Champaign, IL, 2010.
- (33) Chaudhary, K.; Chen, Q.; Juarez, J. J.; Granick, S.; Lewis, J. A. *J. Am. Chem. Soc.* **2012**, *134*, 12901–12903.
- (34) Golestanian, R.; Liverpool, T. B.; Ajdari, A. *New J. Phys.* **2007**, *9*, 126–126.
- (35) Yan, L.-T.; Popp, N.; Ghosh, S.-K.; Böker, A. *ACS Nano* **2010**, *4*, 913–20.
- (36) Mair, L. O.; Evans, B.; Hall, A. R.; Carpenter, J.; Shields, A.; Ford, K.; Millard, M.; Superfine, R. *J. Phys. D: Appl. Phys.* **2011**, *44*, 125001.
- (37) Paxton, W. F.; Kistler, K. C.; Olmeda, C. C.; Sen, A.; St Angelo, S. K.; Cao, Y.; Mallouk, T. E.; Lammert, P. E.; Crespi, V. H. *J. Am. Chem. Soc.* **2004**, *126*, 13424–31.
- (38) Li, X.; Wang, T.; Zhang, J.; Zhu, D.; Zhang, X.; Ning, Y.; Zhang, H.; Yang, B. *ACS Nano* **2010**, *4*, 4350–4360.

- (39) Qin, L.; Park, S.; Huang, L.; Mirkin, C. A. *Science* **2005**, 309, 113–115.
- (40) Kabaso, D.; Gongadze, E.; Elter, P.; van Rienen, U.; Gimsa, J.; Kralj-Iglić, V.; Iglič, a *Mini-Rev. Med. Chem.* **2011**, 11, 272–82.
- (41) Wang, Q.; Navarro, M. V. a S.; Peng, G.; Molinelli, E.; Goh, S. L.; Judson, B. L.; Rajashankar, K. R.; Sondermann, H. *Proc. Natl. Acad. Sci. U.S.A.* **2009**, 106, 12700–5.
- (42) Andelman, D.; Rosensweig, R. E. *J. Phys. Chem. B* **2009**, 113, 3785–3798.
- (43) Fredrickson, G. H. *The Equilibrium Theory of Inhomogeneous Polymers*; Oxford University Press: Oxford, 2006.
- (44) Hansen, J. P.; McDonald, I. R. *Theory of Simple Liquids*; Academic Press: New York, 1986; Vol. 2, p 416.
- (45) Chandler, D.; Andersen, H. C. *J. Chem. Phys.* **1972**, 57, 1930.
- (46) Munaó, G.; Costa, D.; Sciortino, F.; Caccamo, C. *J. Chem. Phys.* **2011**, 134, 194502.
- (47) Schweizer, K. S.; Curro, J. G. *Adv. Chem. Phys.* **1997**, 98, 1–142.
- Guenza, M.; Schweizer, K. S. *J. Chem. Phys.* **1997**, 106, 7391.
- (48) Jayaraman, A.; Schweizer, K. S. *Mol. Simul.* **2009**, 35, 835.
- (49) Leibler, L. *Macromolecules* **1980**, 13, 1602–1617.
- (50) Percus, J. K.; Yevick, G. J. *Phys. Rev.* **1958**, 110, 1–13.
- (51) Fredrickson, G. H.; Helfand, E. *J. Chem. Phys.* **1987**, 87, 697.
- (52) Rubinstein, M.; Colby, R. H. *Polymer Physics*; Oxford University Press: New York, 2003; p 454.
- (53) Bates, F. S.; Fredrickson, G. H. *Phys. Today* **1999**, 52, 32–38.
- (54) Williams, S.; Philipse, A. *Phys. Rev. E* **2003**, 67, 1–9.
- (55) Gast, A. P.; Hall, C. K.; Russel, W. B. *J. Colloid Interface Sci.* **1983**, 96, 251–267.
- (56) Ilett, S. M.; Orrock, A.; Poon, W. C. K.; Pusey, P. N. *Phys. Rev. E* **1995**, 51, 1344–1353.
- (57) Bates, F. S.; Maurer, W. W.; Lipic, P. M.; Hillmyer, M. A.; Almdal, K.; Mortensen, K.; Fredrickson, G. H.; Lodge, T. P. *Phys. Rev. Lett.* **1997**, 79, 849–852.
- (58) Kern, N.; Frenkel, D. *J. Chem. Phys.* **2003**, 118, 9882.
- (59) Ohta, T.; Kawasaki, K. *Macromolecules* **1986**, 19, 2621–2632.
- (60) De Gennes, P.-G. *J. de Physique (Paris)* **1970**, 31, 235–238.
- (61) Schweizer, K. S. *Curr. Opin. Colloid Interface Sci.* **2007**, 12, 297–306.
- (62) Yatsenko, G.; Schweizer, K. S. *Langmuir* **2008**, 24, 7474–7484.
- (63) Tripathy, M.; Schweizer, K. S. *Phys. Rev. E* **2011**, 83, 041406.
- (64) Tripathy, M.; Schweizer, K. S. *Phys. Rev. E* **2011**, 83, 041407.
- (65) Zhang, R.; Schweizer, K. S. *J. Chem. Phys.* **2012**, 136, 154902.